RESEARCH ARTICLE | MARCH 03 2025

Hong–Ou–Mandel interferometry and quantum metrology with multimode frequency-bin entangled photons

Xu Jing ; Linjie Fan ; Xiaodong Zheng; Tangsheng Chen; Yuechan Kong ; Bin Niu ✉ ; Liangliang Lu ✉

APL Photonics 10, 036101 (2025)
https://doi.org/10.1063/5.0250593

APL Photonics ARTICLE pubs.aip.org/aip/app

Hong–Ou–Mandel interferometry and quantum metrology with multimode frequency-bin entangled photons

Cite as: APL Photon. 10, 036101 (2025); doi: 10.1063/5.0250593
Submitted: 26 November 2024 • Accepted: 12 February 2025 •
Published Online: 3 March 2025

View Online Export Citation CrossMark

Xu Jing,[1,2] **Linjie Fan,**[2] **Xiaodong Zheng,**[2] **Tangsheng Chen,**[2] **Yuechan Kong,**[2] **Bin Niu,**[1,2,3,a)] **and Liangliang Lu**[1,2,3,a)]

AFFILIATIONS

[1] Key Laboratory of State Manipulation and Advanced Materials in Provincial Universities, School of Physical Science and Technology, Nanjing Normal University, Nanjing 210023, China
[2] National Key Laboratory of Solid-State Microwave Devices and Circuits, Nanjing Chip Valley Industrial Technology Institute, Nanjing Electronic Devices Institute, Nanjing 210016, China
[3] National Laboratory of Solid-State Microstructures and School of Physics, Nanjing University, Nanjing 210093, China

[a)] **Authors to whom correspondence should be addressed:** niubin_1@126.com and lianglianglu@nju.edu.cn

ABSTRACT

Quantum entanglement is a vital resource in quantum information processing. High-dimensional quantum entanglement offers advantages that classical systems cannot surpass, particularly in enhancing channel capacity, improving system noise resilience, and increasing sensitivity to external environments. The construction of multimode entanglement in the spectral domain is well-suited for fiber-optic systems. Here, we present a straightforward scheme for generating multimode frequency-bin entanglement using a semiconductor chip through a simple mode conversion. A general model for Hong–Ou–Mandel (HOM) interference with a multimode frequency-bin entangled state is presented and applied to the experiments. The multimode entangled photons we produced exhibit HOM interference with a high-visibility beating pattern, demonstrating a strong relationship with the mode number, mode spacing, and the profile of the single mode. Building on the Fisher information analysis, we explore the relationship between the features in multimode entangled state interference traces and the precision of interferometric measurements even in the presence of experimental nonidealities. This work may deepen the understanding of multimode frequency-bin entanglement and advance the application of multimode HOM interference in quantum sensing.

I. INTRODUCTION

Since its discovery, quantum entanglement has posed significant challenges to some of the most well-established perspectives on the nature of the world. Besides its profound significance on the foundations of quantum mechanics, entanglement has found numerous applications in quantum-enhanced technology, including quantum computation,[1] communication,[2] and metrology.[3] The advancement of photonic quantum information processing (QIP) is heavily reliant on high-quality quantum sources. Currently, the most widely used method for generating entangled photons at room temperature is spontaneous parametric down conversion (SPDC) in nonlinear crystals. The popularity of SPDC stems from the relative simplicity of its experimental implementation and the diverse quantum features exhibited by down-converted photons. The photon pair can be entangled in various degrees of freedom (DOF), such as polarization,[4,5] frequency,[6–11] path,[12–16] orbital angular momentum,[17–19] and hybrid polarization-frequency modes.[20–23]

Frequency DOFs have garnered significant interest in recent years due to their ability to convey large-scale quantum information within a single spatial mode and their compatibility with off-the-shelf fiber infrastructure and scalability for high-dimensional QIP applications, including high-capacity quantum communication,[24] multimode quantum storage,[25,26] and quantum frequency processor.[27] Frequency is inherently a continuous DOF, but discrete frequency-bins are often regarded as more advantageous in the framework of QIP.[28–33] A simple discretely color-entangled Bell state is $(|\omega_1\rangle|\omega_2\rangle + |\omega_2\rangle|\omega_1\rangle)/\sqrt{2}$, where ω_1 and ω_2 represent two well-separated frequency bins.[34] Several experimental schemes have been implemented to generate such a color entangled state,[20,22,35–43] which could be used as a promising resource for quantum interference applications. Hong–Ou–Mandel (HOM) interference is a prototypical demonstration of quantum interference,[44–46] whereby two identical photons arriving simultaneously at different input ports of a beam splitter (BS) combine and exit through a single output port. While it is commonly believed that ultrahigh precision in the measurement necessitates ultra-broadband photon sources, it has been demonstrated that HOM interferometry, combined with color-entangled states, can recover the Quantum Cramér–Rao (QCR) bound. This approach is sufficient for attaining high precision, which is primarily determined not by the coherence time of photons, but by the separation of the center frequencies of the state.[43] Alternatively, the timing limits of quantum metrology using the multi-color entangled state, commonly known as biphoton frequency comb (BFC), as a probe state have been investigated.[47] The findings indicate that the QCR bound scales quadratically with the mode number, suggesting that both increased frequency detuning and a larger number of modes in the BFC are beneficial for enhancing the time precision. Recently, by leveraging advances in complementary metal-oxide-semiconductor (CMOS) fabrication techniques, integrated sources have gained prominence as a vital resource for generating BFC to meet the growing demand for advanced non-classical information tasks.[48–50] However, to the best of our knowledge, the versatile generation of multi-color entangled states using chip-based sources, as well as the multimode quantum interference of these states, has not yet been fully explored.

Here, we conduct a comprehensive analysis of the HOM interference characteristics with different multi-color entangled states by using an integrated broadband source, emitting entangled photons at a telecom wavelength band on an AlGaAs semiconductor chip. AlGaAs semiconductor material serves as an exceptional platform due to its strong second-order nonlinearities, high electro-optic coefficient, and minimal birefringence, which facilitates the direct generation of hybrid polarization-frequency entangled states.[51,52] Moreover, as a direct bandgap III–V compound semiconductor, AlGaAs is well suited for lasing, paving the way for the development of monolithic integration of a quantum light source.[53] Based on the AlGaAs Bragg reflection waveguide (BRW), we demonstrate deterministic entanglement-mode conversion between frequency and polarization modes. Furthermore, we report a simple scheme for the generation of multimode frequency-bin entanglement and describe the impact of multimode effects on the HOM interference pattern with a general model. The Fisher information of a real multimode HOM interferometry is evaluated with corresponding probability distributions, indicating that multimode frequency bin entanglement can offer complementary advantages for quantum metrology.

II. THEORY OF FREQUENCY MULTI-MODE HOM INTERFERENCE

Let us consider an experimental configuration where entangled photon pairs are generated through degenerated type-II SPDC from an AlGaAs BRW using a continuous wave pump centered at ω_{p0}. The quantum source achieves phase matching by utilizing bounded total internal reflection (TIR) modes formed between high- and low-index claddings, along with quasi-bounded BRW modes guided through transverse Bragg reflections at the interface between core and period claddings.[51,52,54–56] In this case, the pump photon is *TE*-polarized, and the biphotons are cross-polarized, with one being *TM* and the other being *TE*. In the low pumping regime, the generated hybrid polarization-frequency biphoton state can be written as

$$|\Psi\rangle = \int d\omega_s d\omega_i \big[f_{HV}(\omega_s,\omega_i)|H,\omega_s\rangle|V,\omega_i\rangle + e^{i\phi} f_{VH}(\omega_s,\omega_i)|V,\omega_s\rangle|H,\omega_i\rangle \big], \tag{1}$$

where ϕ is the relative phase and $f_{HV}(\omega_s,\omega_i)$ is the joint spectral amplitude (JSA) of signal and idler photons in horizontal (H) and vertical (V) polarization, respectively (we define $TE = H$, $TM = V$ in waveguide). $f_{VH}(\omega_s,\omega_i)$ has a similar definition. Because of the small birefringence of the AlGaAs material, $f_{HV}(\omega_s,\omega_i)$ can overlap with $f_{VH}(\omega_s,\omega_i)$ over a wide spectral range.[51] Therefore, if we only consider the spectral overlap regions, the two JSAs can be assumed as identical. For ease of discussion and without loss of generality, we further use discretized frequency bins instead of continuous-frequency entanglement and can thus rewrite the state as

$$|\Psi\rangle = \sum_{m=0}^{M} \frac{1}{\sqrt{M+1}} f_m(\nu_s) f_m(\nu_i) \times |\omega_{s,m}+\nu_s\rangle|\omega_{i,m}+\nu_i\rangle \times \Big[|H,\omega_{s,m}\rangle|V,\omega_{i,m}\rangle + e^{i\phi}|V,\omega_{s,m}\rangle|H,\omega_{i,m}\rangle\Big], \tag{2}$$

where m represents the mth frequency-bin pair, as illustrated in Fig. 1. $M+1$ is the total number of frequency-bin pairs, and $\omega_{s/i,m}$ is the center frequency of signal or idler photons, which satisfies the energy conservation condition $\omega_{s,m} + \omega_{i,m} = \omega_{p0}$ with $\omega_{s,0} = \omega_{i,0} = \omega_{p0}/2$. Moreover, we have $\omega_{s,m} = \omega_{s0} - m\Delta\omega$, $\omega_{i,m} = \omega_{i0} + m\Delta\omega$, where $\Delta\omega$ is the free spectral range. $f_m(\nu_s)$ and $f_m(\nu_i)$ are the spectral distributions of the mth signal and idler modes, respectively, and satisfy the normalized condition $\int d\nu_s |f_m(\nu_s)|^2 = \int d\nu_i |f_m(\nu_i)|^2 = 1$. Here, we consider continuous wave pumping, i.e., $\nu_i = -\nu_s = \nu$, and assume that all the mode profiles are the same. As has been reported in Refs. 57–62, by splitting the photons with a dichroic mirror or wavelength division multiplexing (WDM), a polarization entangled state can be obtained,

$$|\Psi_{pol}\rangle = \sum_{m=0}^{M} \frac{1}{\sqrt{M+1}} \int d\nu f(\nu) f(-\nu) \times |\omega_{s,m}-\nu\rangle|\omega_{i,m}+\nu\rangle\Big[|H\rangle|V\rangle + e^{i\phi}|V\rangle|H\rangle\Big]. \tag{3}$$

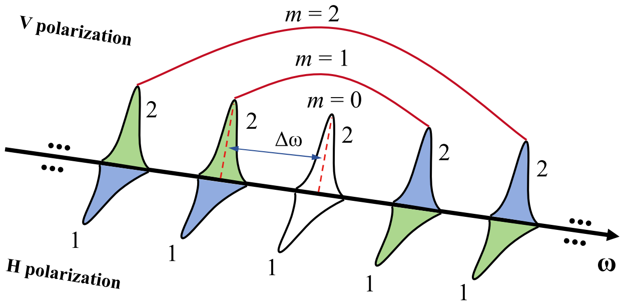

FIG. 1. Multimode frequency-bin entanglement. 1, 2 represent different spatial modes, i.e., the two outputs of the PBS. Red lines represent pairwise entanglement across energy matched bins.

Alternatively, frequency entanglement can be obtained by using a polarizing beam splitter (PBS) to spatially separate the photons in terms of polarization;[20,37] then, the state can be expressed as

$$|\Psi_{freq}\rangle = \sum_{m=0}^{M} \frac{1}{\sqrt{M+1}} \int d\nu f(\nu) f(-\nu) \times \Big[|\omega_{s,m} - \nu\rangle_{1,H} |\omega_{i,m} + \nu\rangle_{2,V} + e^{i\phi} |\omega_{i,m} + \nu\rangle_{1,H} |\omega_{s,m} - \nu\rangle_{2,V} \Big], \tag{4}$$

where 1 and 2 represent the two output spatial modes of the PBS. Thereby, the multimode frequency-bin entanglement as shown in Fig. 1 is generated.

Experimentally, a number of modes with the same line shape can be arbitrarily engineered by a pulse shaper. For simplicity, we set $\phi = 0$ and the mode spectral follows a Gaussian distribution $f(\nu) = f(-\nu) = \kappa e^{-\frac{\nu^2}{2\sigma^2}}$, where κ is the normalization coefficient and σ is the spectral full-width at half-maximum (FWHM) bandwidth for the mode file.[37] We inject each photon of the pair into the two arms of a HOM interferometer, respectively; the two-photon coincidence probability reads

$$P_{cr}(\tau) = \frac{1}{2}\left[1 - \frac{V_\omega}{N} \cdot e^{-\frac{\sigma^2\tau^2}{2}} \cdot \frac{\sin(N\Delta\omega\tau)}{\sin(\Delta\omega\tau)}\right], \tag{5}$$

where N is the total number of modes, V_ω stands for the interference visibility, and τ is the delay introduced in one arm. See the Appendix for more detailed calculations. It indicates that the interferogram exhibits a spatial quantum beating, modulated by the Fourier transform of the spectral distribution of each mode, and is dependent on the number of modes and spectral separation within the frequency comb.

In terms of application, HOM interferometry is immune to variations in the relative phase between the two photons, a property that suggests its potential for sensing schemes requiring precise knowledge of optical delays[63] and tilt angles.[64,65] From classical estimation theory, the ultimate limit of a sensor on the estimation precision of an unknown parameter τ is known as the Cramér–Rao bound, which states the variance of any unbiased estimator $\tilde{\tau}$,[63]

$$\mathrm{Var}(\tilde{\tau}) \geq \frac{1}{Num \cdot F(\tau)}, \tag{6}$$

where Num is the number of measurements and $F(\tau)$ is the Fisher information,

$$F(\tau) = \frac{(\partial P_0(\tau)/\partial\tau)^2}{P_0(\tau)} + \frac{(\partial P_1(\tau)/\partial\tau)^2}{P_1(\tau)} + \frac{(\partial P_2(\tau)/\partial\tau)^2}{P_2(\tau)}, \tag{7}$$

with P_0, P_1, and P_2 represent the probability that no photon, only one photon, and both photons are detected, respectively. The standard deviation of the estimator $\tilde{\tau}$ is lower-bounded by[43]

$$\delta\tau = \frac{1}{\sqrt{Num \cdot F(\tau)}} \geq \delta\tau_{\mathrm{QCR}}. \tag{8}$$

The last inequality in the above equation illustrates that regardless of the optimal measurement strategy employed, it is impossible to achieve a precision that exceeds the QCR bound. Since the QCR bound is closely related to the probe state and specific measurement strategy,[66–68] it is clear that the appropriate choice of experimental configuration is very important. Fortunately, it has been demonstrated that the QCR bound can be recovered by employing color entanglement within the HOM scheme, provided that there is zero loss and perfect visibility.[43] Here, we extend the model for the multimode entangled state. In real experiments, there are always losses and factors that influence the interference visibility. Following Ref. 63, the probability distributions can be modeled as

$$\begin{pmatrix} P_0(\tau) \\ P_1(\tau) \\ P_2(\tau) \end{pmatrix} = \begin{pmatrix} \gamma^2 & \gamma^2 \\ 2\gamma(1-\gamma) & (1-\gamma^2) \\ (1-\gamma)^2 & 0 \end{pmatrix} \begin{pmatrix} P_{cr}(\tau) \\ P_{br}(\tau) \end{pmatrix}, \tag{9}$$

where γ is the lost probability for a photon immediately before detection and $P_{br}(\tau) = 1 - P_{cr}(\tau)$. The resultant probability distributions are

$$P_0(\tau) = \gamma^2, \tag{10}$$

$$P_1(\tau) = 1 - \gamma^2 - \frac{1}{2}(1-\gamma)^2\left[1 - \frac{V_\omega}{N} e^{-\frac{\sigma^2\tau^2}{2}} \frac{\sin(N\Delta\omega\tau)}{\sin(\Delta\omega\tau)}\right], \tag{11}$$

$$P_2(\tau) = \frac{1}{2}(1-\gamma)^2\left[1 - \frac{V_\omega}{N} e^{-\frac{\sigma^2\tau^2}{2}} \frac{\sin(N\Delta\omega\tau)}{\sin(\Delta\omega\tau)}\right], \tag{12}$$

with $P_0(\tau) + P_1(\tau) + P_2(\tau) = 1$. Finally, the Fisher information is given by

$$F(\tau) = \frac{(1-\gamma)^2(1+\gamma)V_\omega{}^2 e^{-\sigma^2\tau^2}\left[N\cos(N\Delta\omega\tau)\Delta\omega - \cot(\Delta\omega\tau)\sin(N\Delta\omega\tau)\Delta\omega - \sigma^2\tau\sin(N\Delta\omega\tau)\right]^2}{(1+3\gamma)N^2\sin^2(\Delta\omega\tau) - (1-\gamma)V_\omega{}^2 e^{-\sigma^2\tau^2}\sin^2(N\Delta\omega\tau) - 4\gamma N sin(\Delta\omega\tau)V_\omega e^{-\frac{\sigma^2\tau^2}{2}}\sin(N\Delta\omega\tau)}. \tag{13}$$

Its upper bound is reached in the limit of $\tau \to 0$, with $\gamma = 0$ and $V_\omega = 1$, and can be expressed as[47]

$$F(\tau) = \frac{(N^2 - 1) \cdot \Delta\omega^2}{3} + \sigma^2. \tag{14}$$

For $N = 2$, it corresponds to that of color-entangled photons with a continuous wave pump.[40,43,69] The dependence of the Fisher information on N and $\Delta\omega$ suggests that multi-mode frequency entanglement with large mode spacing could provide complementary benefits for quantum enhanced metrology.

III. EXPERIMENT AND RESULTS

Figure 2 shows our experimental setup, including three parts: generation of hybrid polarization-frequency entangled photons, polarization entanglement mode conversion (EMC), and frequency EMC. As shown in Fig. 2(a), we use an AlGaAs BRW source to prepare the hybrid entanglement, which can also be realized by other platforms.[20,22,38,70,71] The source consists of stacked AlGaAs layers with alternative aluminum concentrations. It features a core $\mathrm{Al}_{xc}\,\mathrm{Ga}_{1-xc}\mathrm{As}$ layer with $xc = 0.17$ and a thickness of 256-nm, sandwiched between six periodic layers. The Bragg stack is composed of alternating layers of 112-nm high ($\mathrm{Al}_{0.28}\,\mathrm{Ga}_{0.72}\mathrm{As}$) and 566-nm low ($\mathrm{Al}_{0.72}\,\mathrm{Ga}_{0.28}\mathrm{As}$) index layers. The sample is grown along the [001] crystal axis and features with an etch width of 5.5 μm and a depth of 3.5 μm. For a detailed description of the source's working principle, we direct the reader to Ref. 59. The temperature of the waveguide is stabilized by a temperature controller. The source is pumped with a 1 mW polarized continuous wave laser of central wavelength at 775.2-nm with a bandwidth below 180-kHz. Light is coupled into and out of the chip using lens-tapered fibers mounted on high-precision servo motors. The total insertion loss of the chip is ~10 dB, which accounts for both input–output coupling losses and propagation losses in the chip for the TIR modes. Due to energy conservation during the SPDC process, the entangled photons exhibit anti-correlation in their frequencies. We carve the continuous frequency entanglement into separated frequency bins by using a wavelength selective switch (WSS). The residual pump, most photoluminescence from the source, and noise photons from the waveshaper were suppressed by long pass filters (LPFs). The photons are received by two InGaAs avalanche single photon detectors, which operate with 25% detection efficiency, 1.6 kHz dark count rates, and 10 μs dead time.

Before performing multimode HOM interference, we evaluate the entanglement bandwidth of the source. As shown in Fig. 2(b), to verify the polarization entanglement, we post-select

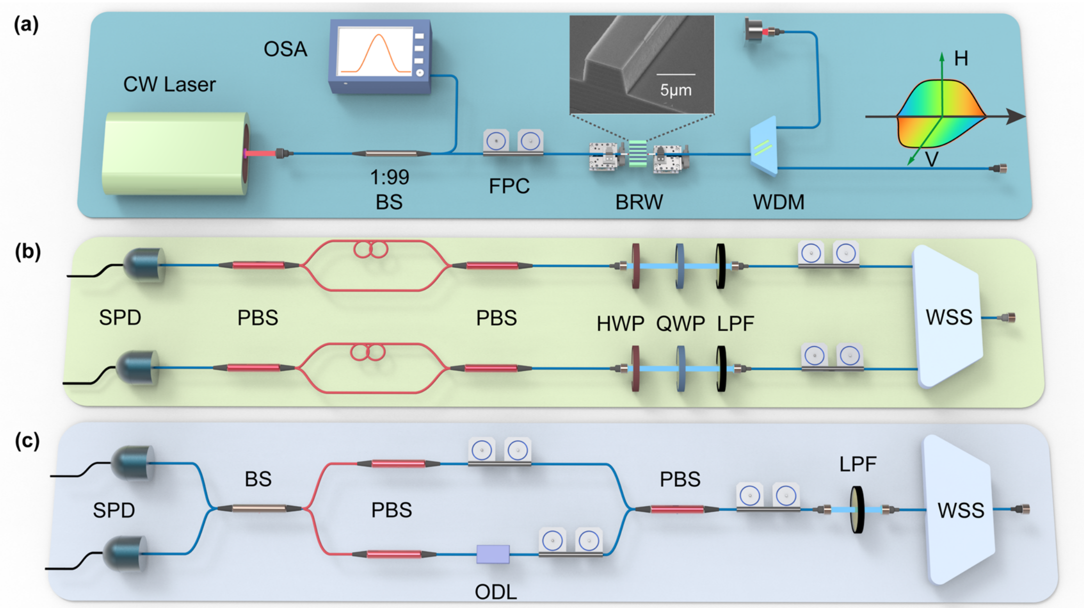

FIG. 2. Experimental setup. (a) Hybrid entanglement source. A 775.2-nm continuous laser is coupled into a fiber and split by a 1:99 BS, where 1% of the light is directed into the optical spectrum analyzer (OSA) for wavelength calibration. The remaining light is polarized by a manual fiber polarization controller (FPC) and coupled into or out of the BRW source by lens-tapered fibers mounted on high-precision servo motors. The rejected pump light filtered by a 980/1550 wavelength division multiplexer (WDM) is utilized as a feedback signal for the motor to stabilize the coupling. The Hill-climbing algorithm is implemented to optimize the coupling under unstable laboratory conditions. The inset shows the scanning electron microscopy image of the fabricated BRW sample. (b) Polarization entanglement generation. The anti-correlated frequencies are post-selected by a wavelength selective switch (WSS). Polarization entanglement is analyzed by measuring interference in Z and X bases. To save the number of single photon detectors (SPDs), the unbalanced polarization-maintaining interferometer is used to introduce a polarization-dependent time delay to distinguish polarization states. (c) Frequency entanglement generation. The hybrid entangled photons are separated with a polarizing beam splitter (PBS) and routed to the input ports of a BS for HOM interference. The delay is introduced by an optical delay line (ODL).

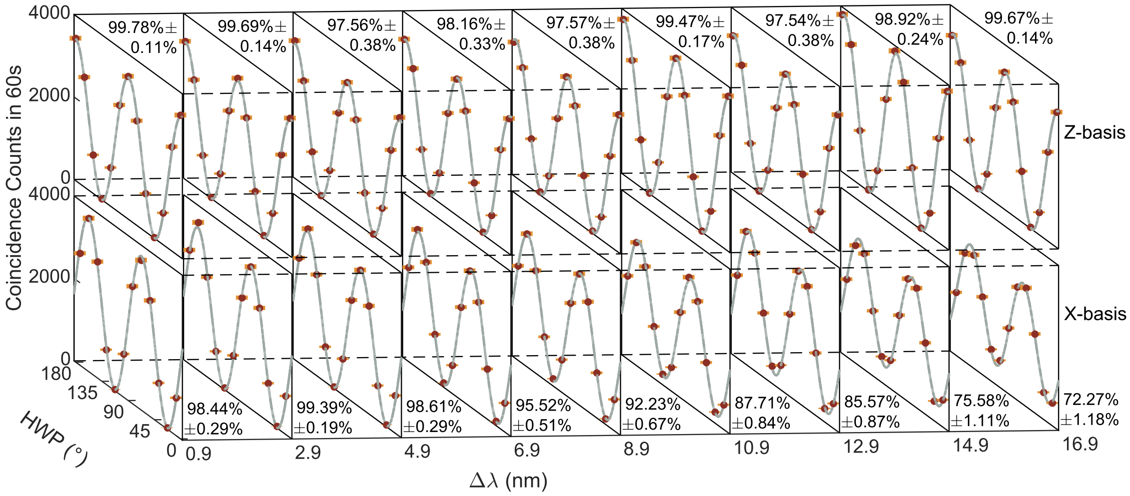

FIG. 3. Interference curves in Z and X bases for nine different channels. The dots are coincidence counts, and the curves are fits, with the visibilities being labeled. The uncertainties denote the standard deviations from the Poisson distribution of the raw photon counts.

symmetric channels concerning the degeneracy wavelength by a WSS and measure the interference curves as a function of the half-wave plate (HWP) angle in Z (HV) and X (DA) bases, where H represents the horizontal polarization and V represents the vertical, and $|D\rangle = \frac{1}{\sqrt{2}}(|H\rangle + |V\rangle)$ and $|A\rangle = \frac{1}{\sqrt{2}}(|H\rangle - |V\rangle)$. To save the number of detectors, the polarization projective measurement primarily uses a fused unbalanced polarization maintaining interferometers, where two polarization modes are separated and combined by two PBSs and with an extra length of polarization-maintaining fiber adding on one of the modes. This enables the transfer of polarization measurement to the time when photons arrive at the detector. We scan an 18-nm passband with a spacing of 2-nm and a bandwidth of 0.8-nm on the WSS and record coincidence counts for each polarization setting, with the single count rate being ~20-kHz. We fix one of the HWPs at the angles of 0° and 22.5°, respectively, and measure the two-photon coincidence counts as a function of another HWP rotation angle. The raw interference curves in Z and X bases are shown in Fig. 3. The measured raw visibilities are presented in Fig. 3 and are defined as $V = (CC_{max} - CC_{min})/(CC_{max} + CC_{min})$, where CC_{max} and CC_{min} are the maximum and minimum of the coincidence counts, respectively, from which the averaged visibilities in the two bases are calculated to estimate the lower bound on the fidelity to the Bell state $|\Psi^{+}\rangle = (|H\rangle|V\rangle + |V\rangle|H\rangle)/\sqrt{2}$.[72] As shown in Fig. 4, the fidelity exceeds 94.6% over a 9-nm range around the degeneracy point, indicating that the JSAs $f_{HV}(\omega_s, \omega_i)$ and $f_{VH}(\omega_s, \omega_i)$ are highly overlapped within this region. The fidelity drop for large detuning with degeneracy wavelength is due to the effect of birefringence occurring in the modes. The bandwidth can be further increased by utilizing shorter waveguides or by designing a structure with sufficiently low group birefringence, which can be achieved through the engineering of material aluminum concentration and waveguide geometries.[52] This type of broadband polarization entangled source has been widely used in multiuser quantum communication networks.[58–60,62]

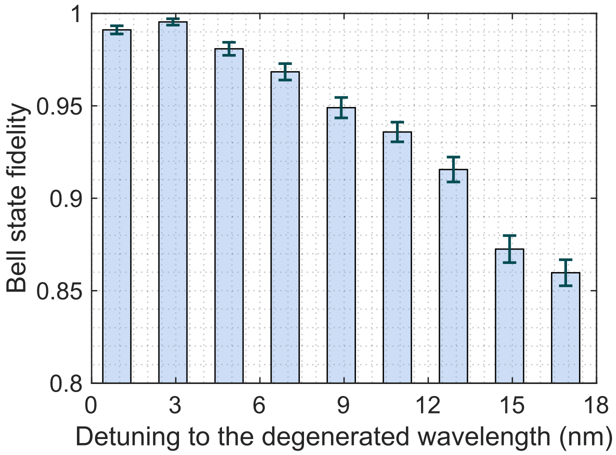

FIG. 4. The lower bound for fidelity to the Bell-state $|\Psi^{+}\rangle$ as a function of the detuning to the biphoton degeneracy wavelength.

Now, we extract multiple frequency bins within a 8-nm range to construct the multimode entangled state expressed in Eq. (4). In general, two photons with distinguishable colors do not exhibit interference in a HOM interferometry since they share no common frequencies (unless the different-color information is erased).[73] Here, the coherent superposition of paired frequency bins is indistinguishable as a joint state and thus can produce a nontrivial interferogram. We choose each mode with a Gaussian profile and introduce delays between the two arms by a 1500 ps motorized delay line. Then, the two photons are mixed at a 50:50 BS and observed by monitoring coincidences between the two output ports of the BS. The coincidence window is set as 300 ps, which exceeds the duration of the filtered photon wavepacket, and the overall delay span. Figure 5 shows the HOM signal for various mode numbers with

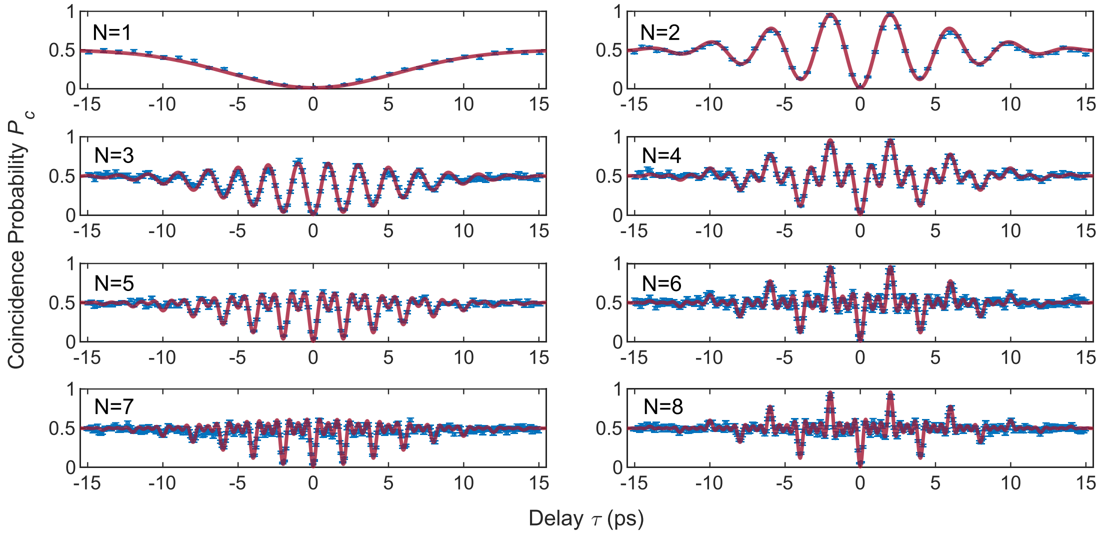

FIG. 5. HOM interference for two-photon multimode frequency-bin entanglement. The number of modes ranges from 1 to 8. The blue dots are the experimental data, and the red lines are the fits of the experimental data according to Eq. (5). The mode interval and mode half-peak width are 250 and 40 GHz, respectively.

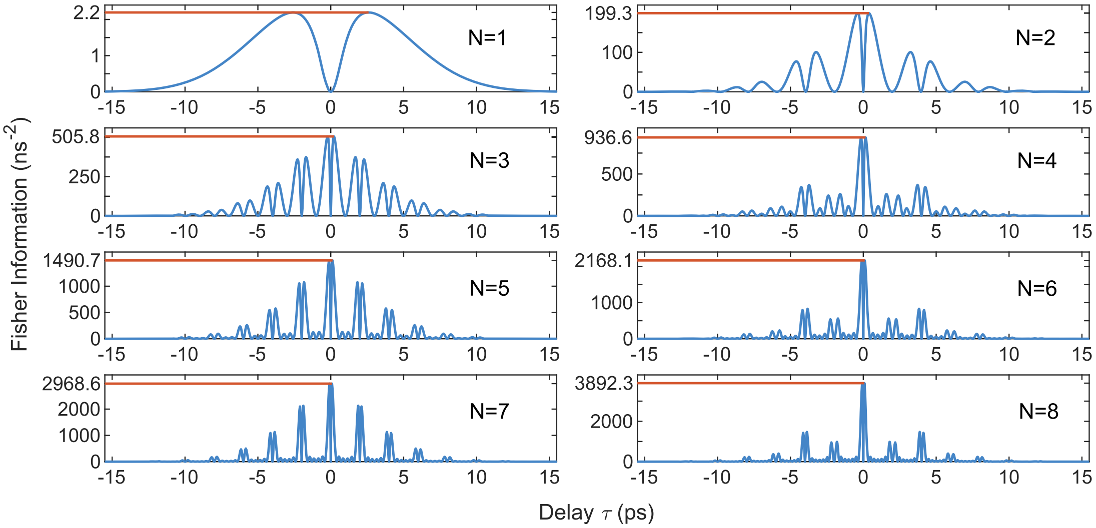

FIG. 6. The Fisher information deduced from experimental results with different mode numbers. The red lines represent the ultimate limits of achievable Fisher information.

the mode spacing and FWHM being 250 and 40-GHz, respectively. The raw counts are normalized with no background counts being subtracted. As can be seen in Fig. 5, the experimental results (dots) align remarkably well with the oscillation shape expected from theory (solid line). From the fitting, we obtain all the visibilities above 0.98, indicating both the stability of the interferometer and the spectral indistinguishability of the photons. For the high-dimensional frequency entanglement, the manifestation of interference fringes can be approximated by the sum of coincidence probabilities of each constituent state with different frequency separations. Following Ref. 74, we can extract the corresponding parameters of a restricted density matrix in the color space by using nonlinear curve-fitting. This approach can be viewed as decomposing the complex periodic vibration into a series of simple harmonic motion. For $N = 8$, deviations of the extracted probability amplitudes from the theoretical value (0.25) are less than 0.03, which confirms that all frequency-bin entangled photons exhibit nearly uniform probability amplitudes. It is also consistent with the fact that the frequency modes are post-selected from the spectral range exhibiting high polarization entanglement as depicted in Fig. 4, indicating that the state is actually close to the form of Eq. (4). Moreover, the even-number interferograms have a symmetric envelope, whereas the odd-number patterns are asymmetric to the line of $P_c = 0.5$,[75] which is caused by the characteristic of the sinusoidal function. There are $N-2$ ($\frac{N-3}{2}$) secondary valleys between two primary valleys for the even (odd) number mode interference patterns. As the number of modes increases, the secondary valley numbers also increase, resulting in a shorter beating oscillation period. While the overall envelop shape remain unchanged, it is solely influenced by the FWHM of the Gaussian line shape. The corresponding Fisher information in experiment is modeled and shown in Fig. 6, from which we note that the increased mode number can facilitate the achievement of higher estimation precision close to $\tau = 0$. The photon loss parameter $\gamma \sim 0.99$ is calculated from the counts according to Ref. 63, which is consistent with the measured data. The loss can be decomposed as follows: the chip-fiber loss is 5 dB (measured by launching light at 1550 nm and collecting the output power from the source), the insertion loss of the WSS and other optical elements is about 9 dB, and the detection loss is 6 dB. Therefore, there is a substantial scope to further increase the Fisher information of our experiment

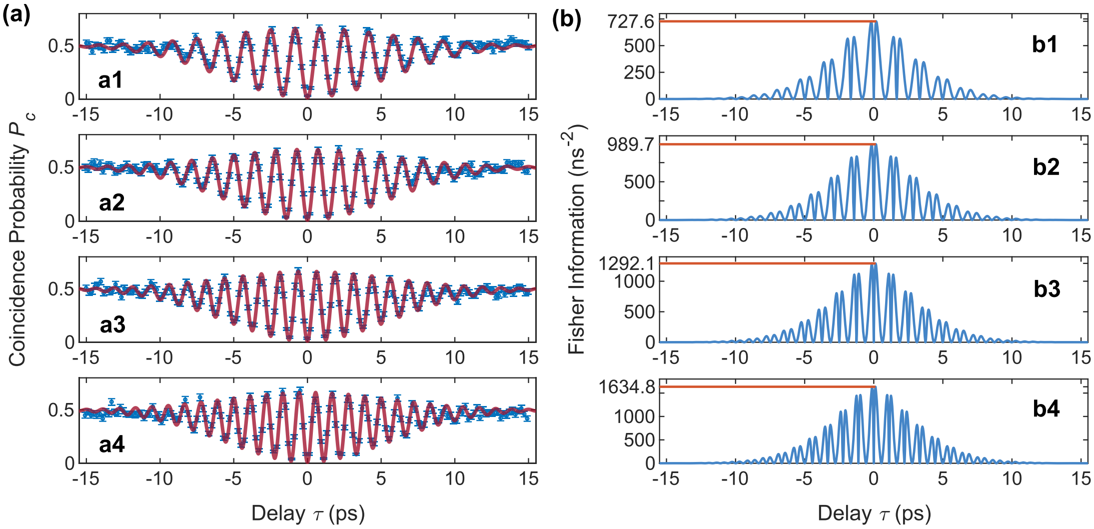

FIG. 7. HOM interference for two-photon multimode frequency-bin entanglement with different mode spacing for $N = 3$. The mode spacings are as follows: (a1) 300-GHz, (a2) 350-GHz, (a3) 400-GHz, and (a4) 450-GHz, respectively. (b1)–(b4) The corresponding Fisher information deduced from experimental results. The red lines represent the ultimate limits of achievable Fisher information.

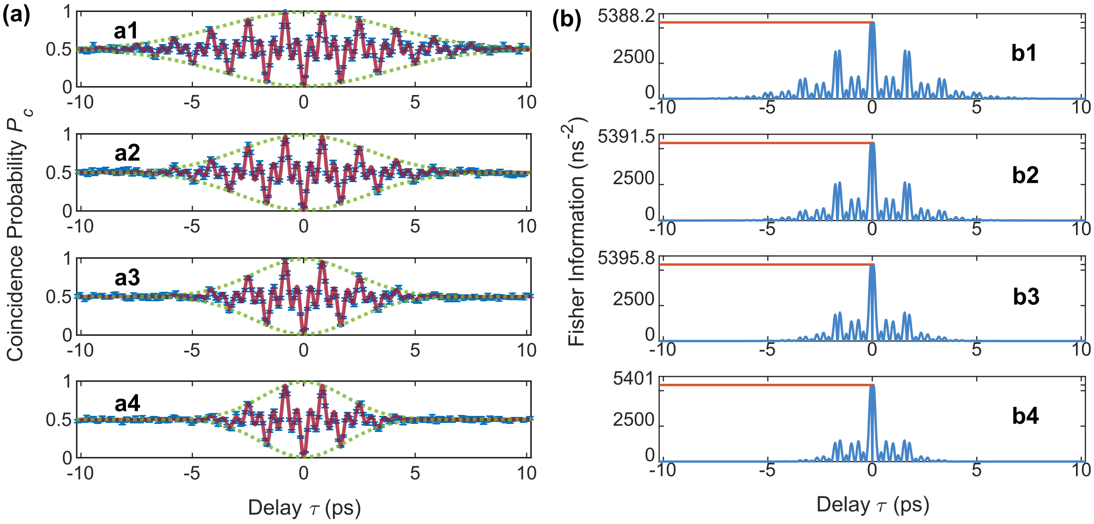

FIG. 8. HOM interference for two-photon multimode frequency-bin entanglement with different mode FWHM for $N = 4$. The mode FWHMs are as follows: (a1) 60-GHz, (a2) 80-GHz, (a3) 100-GHz, and (a4) 120-GHz, respectively. The dashed curve in each figure represents the theoretical envelope determined by each mode. (b1)–(b4) The corresponding Fisher information calculated from experimental results. The red lines represent the ultimate limits of achievable Fisher information.

through optimizing the coupling and using higher efficiency detectors. It is worth mentioning that, although the interferogram is the incoherent sum of different frequency pairs,[37] collecting more modes simultaneously allows the total acquisition time to be reduced for each measurement.

Next, we study the influence of mode spacing on multimode HOM interference. The mode number is fixed at 3, and the FWHM is set to 40-GHz. As shown in Figs. 7(a1)–7(a4), as the mode spacing increases, the oscillation period decreases, which is alike the increase in the number of modes. That is because the mode spacing $\Delta\omega$ directly affects the oscillation term in Eq. (5). This is visually represented by an increase in the number of peaks within the same time variable range (determined by the FWHM), accompanied by a decrease in the width of the oscillation. The corresponding Fisher information is also shown in Figs. 7(b1)–7(b4), indicating that larger frequency difference produces higher precision. We further consider the effects of mode FWHM in Fig. 8 when the mode number of modes is set to 4 and the mode spacing is 600-GHz. We can observe that as the FWHM increases, the oscillation period remains constant, while the overall envelop decreases Figs. 8(a1)–8(a4). This is manifested as the correlation time of the photons is typically defined as the inverse of the mode width, i.e., $t_{coh} \propto 1/\sigma$. When the time difference Δt between the arrival of the two photons at the detectors is much greater than t_{coh} (i.e., $\Delta t \gg t_{coh}$), the coincidence counting approaches its trivial value 0.5. Therefore, as σ increases, t_{coh} decreases, leading to the coincidence probability reaching the trivial value earlier, which is reflected in the reduction of the envelope range. The constant oscillation period also indicates that the maximal Fisher information is almost unchanged [Figs. 8(b1)–8(b4)].

IV. CONCLUSION

In summary, we have demonstrated the direct generation of broadband hybrid entanglement between polarization and frequency in a semiconductor AlGaAs chip and realized deterministic entanglement-mode conversion between the two DOFs. Such an entangled source possesses a high degree of flexibility, allowing it to be adapted to different platforms tailored to practical QIP applications. In particular, we prepare multimode frequency-bin entanglement and investigate its characteristics in HOM interferometry. The scheme maintains cross-bin entanglement while exhibiting high spectral purity within each bin, making them valuable for heralding pure single photons. The interferogram is determined by three parameters: the mode number, mode spacing, and the profile of each frequency bin. The first two parameters affect the biphoton beating oscillation, while the last parameter influences the shape of the overall envelope. To further assess the impact of multi-mode entangled states on measurement precision, we quantified measurement accuracy using Fisher information, which can recover the QCR bound in ideal HOM interference. The results indicate that as the number of modes or the mode spacing increases, the precision also improves, as reflected in the internal oscillation factors. Therefore, multiple well-separated and entangled discrete frequency modes may facilitate the use of HOM interference for quantum sensing. Notably, although we achieved the multimode frequency bins through post-selection at the cost of photon flux, the trade-off can be overcome via spectral compression with time-varying cavities.[76,77] Our results underscore the significance of state preparation in the applications of quantum theory and offer new insights into HOM-based quantum sensors.

ACKNOWLEDGMENTS

This work was supported by the National Natural Science Foundation of China (Grant No. 12274233) and Nanjing Electronic Devices Institute (Grant No. 2311N051).

AUTHOR DECLARATIONS

Conflict of Interest

The authors have no conflicts to disclose.

Author Contributions

X. J., L.-J. F., and X.-D. Z. contributed equally to this work.

Xu Jing: Conceptualization (equal); Data curation (equal); Funding acquisition (equal); Investigation (equal); Methodology (equal); Project administration (equal); Supervision (equal); Writing – original draft (equal); Writing – review & editing (equal). **Linjie Fan**: Data curation (equal); Investigation (equal); Methodology (equal); Writing – original draft (equal). **Xiaodong Zheng**: Investigation (supporting); Methodology (equal); Writing – original draft (equal); Writing – review & editing (equal). **Tangsheng Chen**: Investigation (supporting); Project administration (equal); Writing – review & editing (equal). **Yuechan Kong**: Project administration (equal). **Bin Niu**: Investigation (equal); Project administration (equal). **Liangliang Lu**: Conceptualization (equal); Funding acquisition (equal); Investigation (equal); Project administration (equal); Supervision (equal); Writing – review & editing (equal).

DATA AVAILABILITY

Data underlying the results presented in this paper are not publicly available at this time but may be obtained from the corresponding authors upon reasonable request.

APPENDIX: CALCULATION OF MULTIMODE HOM INTERFERENCE

In this section, we show the calculation of the multimode frequency-bin entanglement HOM interference. We ignore polarization subscripts for convenience and use $\hat{a}_1^+(\omega_0 \pm \Omega)$, $\hat{a}_2^+(\omega_0 \pm \Omega)$ to represent photon generation operators in different spatial modes, where $\omega_0 = \omega_{p0}/2$. Consider the single-mode frequency-bin entangled state with Gaussian distribution,

$$\begin{aligned}|\psi_m\rangle &= \int d\nu \cdot \kappa e^{-\frac{\nu^2}{\sigma^2}} \big[\, |\omega_{s,m} - \nu\rangle_{1,H} |\omega_{i,m} + \nu\rangle_{2,V} \\ &\quad + e^{i\phi} |\omega_{i,m} + \nu\rangle_{1,H} |\omega_{s,m} - \nu\rangle_{2,V} \,\big] \\ &= \int d\Omega \cdot \kappa e^{-\frac{(\Omega-\Omega_m)^2}{\sigma^2}} \big[\, \hat{a}_1^+(\omega_0 - \Omega) \hat{a}_2^+(\omega_0 + \Omega) \\ &\quad + e^{i\phi} \hat{a}_1^+(\omega_0 + \Omega) \hat{a}_2^+(\omega_0 - \Omega) \,\big] |vac\rangle, \end{aligned} \tag{A1}$$

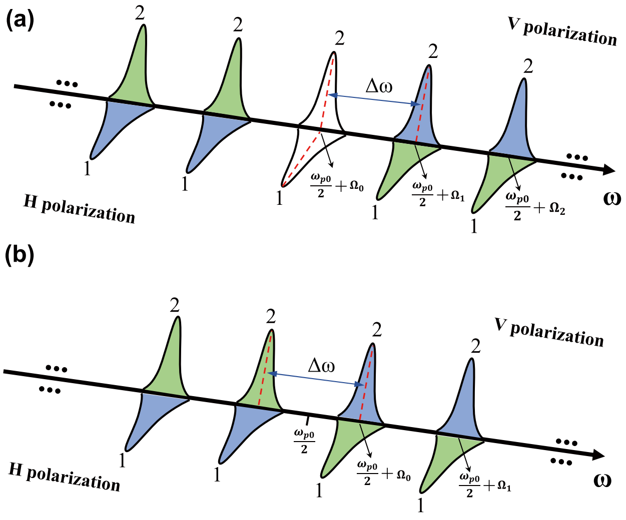

FIG. 9. Multimode frequency-bin entanglement. 1, 2 represent different spatial modes, i.e., the two outputs of the PBS and the central frequency for each bin are $\omega_{p0}/2 + \Omega_m$. The number of modes is divided into odd (a), where $\Omega_m = m\Delta\omega$, and even (b), where $\Omega_m = \left(m + \frac{1}{2}\right)\Delta\omega$, with respect to $\omega_{p0}/2$ to ensure that the interval between each mode is kept at $\Delta\omega$.

where $\nu = \Omega - \Omega_m$ and κ is the normalization coefficient. To keep a consistent interval of $\Delta\omega$ between each mode, we set $\Omega_m = m\Delta\omega$ for odd modes [Fig. 9(a)], $\Omega_m = \left(m + \frac{1}{2}\right)\Delta\omega$ for even modes [Fig. 9(b)].

The scheme of the interferometry is shown in Fig. 10, where the field operators at detectors D3 and D4 can be expressed as

$$\hat{E}^{+}_{D3}(t) = \int e^{-i\omega_3 t}\hat{a}_3(\omega_3)d\omega_3, \tag{A2}$$

$$\hat{E}^{+}_{D4}(t) = \int e^{-i\omega_4 t}\hat{a}_4(\omega_4)d\omega_4, \tag{A3}$$

where $\hat{a}_3(\omega_3)$ and $\hat{a}_4(\omega_4)$ are the photon annihilation operators of the two detectors. After the delay τ is introduced in one arm, the balanced BS can transform the operator as

$$\hat{a}_3(\omega_3) = \left(e^{i\omega_3\tau}\hat{a}_1(\omega_3) - \hat{a}_2(\omega_3)\right)/\sqrt{2}, \tag{A4}$$

$$\hat{a}_4(\omega_4) = \left(e^{i\omega_4\tau}\hat{a}_1(\omega_4) + \hat{a}_2(\omega_4)\right)/\sqrt{2}. \tag{A5}$$

Then, we can represent the detector field operator in terms of $\hat{a}_1$ and $\hat{a}_2$ operators,

$$\hat{E}^{+}_{D3}(t) = \frac{1}{\sqrt{2}}\int d\omega_3\left[e^{i\omega_3(\tau-t)}\hat{a}_1(\omega_3) - e^{-i\omega_3 t}\hat{a}_2(\omega_3)\right], \tag{A6}$$

$$\hat{E}^{+}_{D4}(t) = \frac{1}{\sqrt{2}}\int d\omega_4\left[e^{i\omega_4(\tau-t)}\hat{a}_1(\omega_4) + e^{-i\omega_4 t}\hat{a}_2(\omega_4)\right]. \tag{A7}$$

The coincidence probability of the two detectors at the time interval Δt can be expressed as[37]

$$P_c = \frac{1}{M+1}\sum_{m=0}^{M}\int_{\Delta t}dt\int_{T_R}dT\left|\langle vac|\hat{E}^{+}_{D3}(t+T)\hat{E}^{+}_{D4}(t)|\psi_m\rangle\right|^2, \tag{A8}$$

where $M + 1$ is the total number of bin pairs and T_R is the resolution time of the detector, which is large compared to the duration of the wave packet.

Since

$$\hat{a}_1(\omega_3)\hat{a}_1(\omega_4)\hat{a}^{\dagger}_1(\omega_0 \mp \Omega)\hat{a}^{\dagger}_2(\omega_0 \pm \Omega)|vac\rangle = 0, \tag{A9}$$

$$\hat{a}_2(\omega_4)\hat{a}_2(\omega_4)\hat{a}^{\dagger}_1(\omega_0 \mp \Omega)\hat{a}^{\dagger}_2(\omega_0 \pm \Omega)|vac\rangle = 0, \tag{A10}$$

then only two terms exist for formula $\langle vac|\hat{E}^{+}_{D3}(t+T)\hat{E}^{+}_{D4}(t)|\psi_m\rangle$. The first term is

$$\begin{aligned}
&\langle vac|\frac{1}{2}\int d\omega_3 e^{i\omega_3(\tau-t-T)}\hat{a}_1(\omega_3)\cdot\int d\omega_4 e^{-i\omega_4 t}\hat{a}_2(\omega_4)|\psi_m\rangle\\
&= \langle vac|\frac{1}{2}\int d\omega_3 e^{i\omega_3(\tau-t-T)}\hat{a}_1(\omega_3)\cdot\int d\omega_4 e^{-i\omega_4 t}\hat{a}_2(\omega_4)\\
&\quad\times\int d\Omega\cdot\kappa e^{-\frac{(\Omega-\Omega_m)^2}{\sigma^2}}\cdot\left[\hat{a}^{\dagger}_1(\omega_0-\Omega)\hat{a}^{\dagger}_2(\omega_0+\Omega) + e^{i\phi}\hat{a}^{\dagger}_1(\omega_0+\Omega)\hat{a}^{\dagger}_2(\omega_0-\Omega)\right]|vac\rangle\\
&= \frac{1}{2}\int d\Omega\cdot\kappa e^{-\frac{(\Omega-\Omega_m)^2}{\sigma^2}}\left(e^{i(\omega_0-\Omega)(\tau-t-T)}e^{-i(\omega_0+\Omega)t} + e^{i\phi}e^{i(\omega_0+\Omega)(\tau-t-T)}e^{-i(\omega_0-\Omega)t}\right)\\
&= \frac{1}{2}\int d\Omega\cdot\kappa e^{-\frac{(\Omega-\Omega_m)^2}{\sigma^2}}\left(e^{-i2\omega_0 t}e^{-i(\omega_0-\Omega)T}e^{i(\omega_0-\Omega)\tau} + e^{i\phi}e^{-i2\omega_0 t}e^{-i(\omega_0+\Omega)T}e^{i(\omega_0+\Omega)\tau}\right).
\end{aligned} \tag{A11}$$

In the above calculation, we use the following relationship:

$$\hat{a}_1(\omega_3)\hat{a}_2(\omega_4)\hat{a}^{\dagger}_1(\omega_0 \mp \Omega)\hat{a}^{\dagger}_2(\omega_0 \pm \Omega)|vac\rangle = \delta(\omega_3 - (\omega_0 \mp \Omega))\delta(\omega_4 - (\omega_0 \pm \Omega)). \tag{A12}$$

The second term is

$$\begin{aligned}\langle vac| - \frac{1}{2}\int d\omega_3 e^{-i\omega_3(t+T)}\hat{a}_2(\omega_3)\int d\omega_4 e^{i\omega_4(\tau-t)}\hat{a}_1(\omega_4)|\psi_m\rangle &= \langle vac| - \frac{1}{2}\int d\omega_3 e^{-i\omega_3(t+T)}\hat{a}_2(\omega_3)\int d\omega_4 e^{i\omega_4(\tau-t))}\hat{a}_1(\omega_4)\\ &\quad\times\int d\Omega\cdot\kappa e^{-\frac{(\Omega-\Omega_m)^2}{\sigma^2}}\cdot\Big[\hat{a}_1^+(\omega_0-\Omega)\hat{a}_2^+(\omega_0+\Omega)+e^{i\phi}\hat{a}_1^+(\omega_0+\Omega)\hat{a}_2^+(\omega_0-\Omega)\Big]|vac\rangle\\ &= -\frac{1}{2}\int d\Omega\cdot\kappa e^{-\frac{(\Omega-\Omega_m)^2}{\sigma^2}}\Big(e^{-i(\omega_0+\Omega)(t+T)}e^{i(\omega_0-\Omega)(\tau-t))}+e^{i\phi}e^{-i(\omega_0-\Omega)(t+T)}e^{i(\omega_0+\Omega)(\tau-t))}\Big)\\ &= -\frac{1}{2}\int d\Omega\cdot\kappa e^{-\frac{(\Omega-\Omega_m)^2}{\sigma^2}}\Big(e^{-i2\omega_0 t}e^{-i(\omega_0+\Omega)T}e^{i(\omega_0-\Omega)\tau}+e^{i\phi}e^{-i2\omega_0 t}e^{-i(\omega_0-\Omega)T}e^{i(\omega_0+\Omega)\tau}\Big).\end{aligned} \tag{A13}$$

In the above calculation, we use the following relationship:

$$\hat{a}_1(\omega_4)\hat{a}_2(\omega_3)\hat{a}_1^+(\omega_0\mp\Omega)\hat{a}_2^+(\omega_0\pm\Omega)|vac\rangle = \delta(\omega_4-(\omega_0\mp\Omega))\delta(\omega_3-(\omega_0\pm\Omega)). \tag{A14}$$

Then, we can obtain

$$\begin{aligned}\langle vac|\hat{E}_{D3}^+(t+T)\hat{E}_{D4}^+(t)|\psi_m\rangle &= \frac{1}{2}\int d\Omega\cdot\kappa e^{-\frac{(\Omega-\Omega_m)^2}{\sigma^2}}\times e^{-i2\omega_0 t}\Big(e^{i(\omega_0-\Omega)\tau}-e^{i\phi}e^{i(\omega_0+\Omega)\tau}\Big)\\ &\quad\times\Big(e^{-i(\omega_0-\Omega)T}-e^{-i(\omega_0+\Omega)T}\Big).\end{aligned} \tag{A15}$$

Inserting Eq. (A15) into Eq. (A8), the coincidence probability can be expressed as

$$\begin{aligned}P_c &= \sum_{m=0}^{M}\frac{1}{M+1}\int_{\Delta t}dt\int_{T_R}dT\left|\frac{1}{2}\int d\Omega\cdot\kappa e^{-\frac{(\Omega-\Omega_m)^2}{\sigma^2}}\cdot e^{-i2\omega_0 t}\Big(e^{i(\omega_0-\Omega)\tau}-e^{i\phi}e^{i(\omega_0+\Omega)\tau}\Big)\Big(e^{-i(\omega_0-\Omega)T}-e^{-i(\omega_0+\Omega)T}\Big)\right|^2\\ &= \sum_{m=0}^{M}\frac{1}{4(M+1)}\int_{T_R}dT\cdot\kappa^2\int d\Omega\cdot\int d\Omega'\cdot e^{-\frac{(\Omega-\Omega_m)^2}{\sigma^2}}e^{-\frac{(\Omega'-\Omega_m)^2}{\sigma^2}}\Big(e^{i(\omega_0-\Omega)\tau}-e^{i\phi}e^{i(\omega_0+\Omega)\tau}\Big)\\ &\quad\times\Big(e^{-i(\omega_0-\Omega)T}-e^{-i(\omega_0+\Omega)T}\Big)\Big(e^{-i(\omega_0-\Omega')\tau}-e^{-i\phi}e^{-i(\omega_0+\Omega')\tau}\Big)\Big(e^{i(\omega_0-\Omega')T}-e^{i(\omega_0+\Omega')T}\Big)\\ &= \sum_{m=0}^{M}\frac{1}{4(M+1)}\int_{T_R}dT\cdot\kappa^2\int d\Omega\cdot\int d\Omega'\cdot e^{-\frac{(\Omega-\Omega_m)^2}{\sigma^2}}e^{-\frac{(\Omega'-\Omega_m)^2}{\sigma^2}}\\ &\quad\times\Big(e^{i(\Omega'-\Omega)\tau}+e^{-i(\Omega'-\Omega)\tau}-e^{-i\phi}e^{-i(\Omega'+\Omega)\tau}-e^{i\phi}e^{i(\Omega'+\Omega)\tau}\Big)\Big(e^{i(\Omega'-\Omega)T}+e^{-i(\Omega'-\Omega)T}-e^{-i(\Omega'+\Omega)T}-e^{i(\Omega'+\Omega)T}\Big)\\ &= \sum_{m=0}^{M}\frac{1}{4(M+1)}\int d\Omega\cdot\kappa^2 e^{-\frac{2(\Omega-\Omega_m)^2}{\sigma^2}}\Big(2-\Big(e^{i\phi}e^{2i\Omega\tau}+e^{-i\phi}e^{-2i\Omega\tau}\Big)\Big)\\ &= \sum_{m=0}^{M}\frac{1}{2(M+1)}\left[1-\int d\Omega\cdot\kappa^2 e^{-\frac{2(\Omega-\Omega_m)^2}{\sigma^2}}\cos(2\Omega\tau+\phi)\right]\left(\int d\Omega\cdot\kappa^2 e^{-\frac{2(\Omega-\Omega_n)^2}{\sigma^2}}=1\right)\\ &= \frac{1}{2}\left[1-\sum_{m=0}^{M}\frac{1}{(M+1)}\int d\Omega\cdot\kappa^2 e^{-\frac{2(\Omega-\Omega_m)^2}{\sigma^2}}\cos(2\Omega\tau+\phi)\right] = \frac{1}{2}\left[1-\sum_{m=0}^{M}\frac{1}{(M+1)}\int d\Omega\cdot\kappa^2 e^{-\frac{2\Omega^2}{\sigma^2}}\cos[2(\Omega+\Omega_m)\tau+\phi]\right]\\ &= \frac{1}{2}\left[1-\sum_{m=0}^{M}\frac{1}{(M+1)}\int d\Omega\cdot\kappa^2 e^{-\frac{2\Omega^2}{\sigma^2}}[\cos(2\Omega\tau)\cos(2\Omega_m\tau+\phi)-\sin(2\Omega\tau)\sin(2\Omega_m\tau+\phi)]\right]\\ &= \frac{1}{2}\left[1-\sum_{m=0}^{M}\frac{1}{(M+1)}\int d\Omega\cdot\kappa^2 e^{-\frac{2\Omega^2}{\sigma^2}}\cos(2\Omega\tau)\cos(2\Omega_m\tau+\phi)\right]\\ &= \begin{cases}\dfrac{1}{2}\left[1-\dfrac{1}{M+\frac{1}{2}}\cdot e^{-\frac{\sigma^2\tau^2}{2}}\cdot\dfrac{\sin((2M+1)\Delta\omega\tau+\phi)+\sin(\Delta\omega\tau-\phi)}{2\sin(\Delta\omega\tau)}\right] & \textit{for odd modes,}\\ \dfrac{1}{2}\left[1-\dfrac{1}{M+1}\cdot e^{-\frac{\sigma^2\tau^2}{2}}\cdot\dfrac{\sin(2(M+1)\Delta\omega\tau+\phi)-\sin(\phi)}{2\sin(\Delta\omega\tau)}\right] & \textit{for even modes.}\end{cases}\end{aligned} \tag{A16}$$

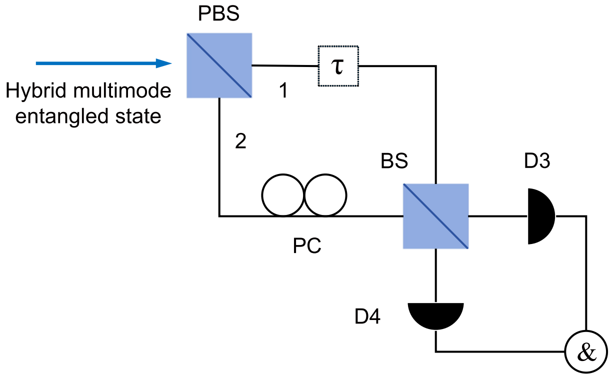

FIG. 10. Typical setup of HOM interference. Signal photons and idle photons are generated by type-II SPDC, in which we introduce a time delay for the subsequent analysis of the time resolution of multimode HOM interference. The photons and idle photons are detected in the output state passing through the BS by two SPDs connected to a coincidence counter.

In the process of calculating odd modes above, we assume

$$|\psi_0\rangle = \int d\Omega \cdot \kappa e^{-\frac{(\Omega-\Omega_0)^2}{\sigma^2}} \cdot [\, a^{+}(\omega_0+\Omega) b^{+}(\omega_0-\Omega) + e^{i\phi} a^{+}(\omega_0-\Omega) b^{+}(\omega_0+\Omega)\,]|vac\rangle. \tag{A17}$$

Specially, for $m = 0$, the state should be

$$|\psi_0\rangle = \int d\Omega \cdot \kappa e^{-\frac{(\Omega-\Omega_0)^2}{\sigma^2}} \times e^{i\phi} a^{+}(\omega_0-\Omega) b^{+}(\omega_0+\Omega)\,]|vac\rangle. \tag{A18}$$

Then, the coincidence probability for the odd mode number needs to be corrected as follows:

$$P_c(\tau) = \frac{1}{2}\left[1 - \frac{1}{M+\frac{1}{2}} \cdot e^{-\frac{\sigma^2\tau^2}{2}} \cdot \frac{\sin\left((2M+1)\Delta\omega\tau+\phi\right) - \sin(\phi)\cos(\Delta\omega\tau)}{2\sin(\Delta\omega\tau)}\right]. \tag{A19}$$

Considering the experimental setup $\phi = 0$ and imperfect interference visibility V_ω, the final coincidence probability can be expressed as follows:

$$P_{cr}(\tau) = \begin{cases} \frac{1}{2}\left[1 - \frac{V_\omega}{M+\frac{1}{2}} \cdot e^{-\frac{\sigma^2\tau^2}{2}} \cdot \frac{\sin\left((2M+1)\Delta\omega\tau\right)}{2\sin(\Delta\omega\tau)}\right] & for\ odd\ modes, \\ \frac{1}{2}\left[1 - \frac{V_\omega}{M+1} \cdot e^{-\frac{\sigma^2\tau^2}{2}} \cdot \frac{\sin\left(2(M+1)\Delta\omega\tau\right)}{2\sin(\Delta\omega\tau)}\right] & for\ even\ modes. \end{cases} \tag{A20}$$

Finally, we denote the total number of modes as N, which is $N = 2M + 1$ $(N = 2M + 2)$ when N is an odd (even) number. This allows us to unify the expression for the coincidence probability,

$$P_{cr}(\tau) = \frac{1}{2}\left[1 - \frac{V_\omega}{N} \cdot e^{-\frac{\sigma^2\tau^2}{2}} \cdot \frac{\sin(N\Delta\omega\tau)}{\sin(\Delta\omega\tau)}\right]. \tag{A21}$$

REFERENCES

[1] T. D. Ladd, F. Jelezko, R. Laflamme, Y. Nakamura, C. Monroe, and J. L. O'Brien, "Quantum computers," Nature **464**, 45 (2010).

[2] N. Gisin, G. Ribordy, W. Tittel, and H. Zbinden, "Quantum cryptography," Rev. Mod. Phys. **74**, 145 (2002).

[3] V. Giovannetti, S. Lloyd, and L. Maccone, "Advances in quantum metrology," Nat. Photonics **5**, 222 (2011).

[4] R. Ikuta, Y. Kusaka, T. Kitano, H. Kato, T. Yamamoto, M. Koashi, and N. Imoto, "Wide-band quantum interface for visible-to-telecommunication wavelength conversion," Nat. Commun. **2**, 537 (2011).

[5] X.-C. Yao, T.-X. Wang, P. Xu, H. Lu, G.-S. Pan, X.-H. Bao, C.-Z. Peng, C.-Y. Lu, Y.-A. Chen, and J.-W. Pan, "Observation of eight-photon entanglement," Nat. Photonics **6**, 225 (2012).

[6] Z. Xie, T. Zhong, S. Shrestha, X. Xu, J. Liang, Y.-X. Gong, J. C. Bienfang, A. Restelli, J. H. Shapiro, F. N. C. Wong, and C. Wei Wong, "Harnessing high-dimensional hyperentanglement through a biphoton frequency comb," Nat. Photonics **9**, 536 (2015).

[7] M. Kues, C. Reimer, P. Roztocki, L. R. Cortés, S. Sciara, B. Wetzel, Y. Zhang, A. Cino, S. T. Chu, B. E. Little *et al.*, "On-chip generation of high-dimensional entangled quantum states and their coherent control," Nature **546**, 622 (2017).

[8] P. Imany, J. A. Jaramillo-Villegas, O. D. Odele, K. Han, D. E. Leaird, J. M. Lukens, P. Lougovski, M. Qi, and A. M. Weiner, "50-GHz-spaced comb of high-dimensional frequency-bin entangled photons from an on-chip silicon nitride microresonator," Opt. Express **26**, 1825 (2018).

[9] X. Cheng, K.-C. Chang, M. C. Sarihan, A. Mueller, M. Spiropulu, M. D. Shaw, B. Korzh, A. Faraon, F. N. C. Wong, J. H. Shapiro, and C. W. Wong, "High-dimensional time-frequency entanglement in a singly-filtered biphoton frequency comb," Commun. Phys. **6**, 278 (2023).

[10] R.-B. Jin and R. Shimizu, "Extended Wiener–Khinchin theorem for quantum spectral analysis," Optica **5**, 93 (2018).

[11] B. Li, C. Chen, B. Yuan, X. Zhang, R. Dong, S. Zhang, and R.-B. Jin, "Full characterization of biphotons with a generalized quantum interferometer," Phys. Rev. A **109**, 043703 (2024).

[12] J. W. Silverstone, D. Bonneau, K. Ohira, N. Suzuki, H. Yoshida, N. Iizuka, M. Ezaki, C. M. Natarajan, M. G. Tanner, R. H. Hadfield *et al.*, "On-chip quantum interference between silicon photon-pair sources," Nat. Photonics **8**, 104 (2014).

[13] H. Jin, P. Xu, X. W. Luo, H. Y. Leng, Y. X. Gong, W. J. Yu, M. L. Zhong, G. Zhao, and S. N. Zhu, "Compact engineering of path-entangled sources from a monolithic quadratic nonlinear photonic crystal," Phys. Rev. Lett. **111**, 023603 (2013).

[14] J. Wang, S. Paesani, Y. Ding, R. Santagati, P. Skrzypczyk, A. Salavrakos, J. Tura, R. Augusiak, L. Mančinska, D. Bacco *et al.*, "Multidimensional quantum entanglement with large-scale integrated optics," Science **360**, 285 (2018).

[15] X. Qiang, X. Zhou, J. Wang, C. M. Wilkes, T. Loke, S. O'Gara, L. Kling, G. D. Marshall, R. Santagati, T. C. Ralph *et al.*, "Large-scale silicon quantum photonics implementing arbitrary two-qubit processing," Nat. Photonics **12**, 534 (2018).

[16] L. Lu, L. Xia, Z. Chen, L. Chen, T. Yu, T. Tao, W. Ma, Y. Pan, X. Cai, Y. Lu *et al.*, "Three-dimensional entanglement on a silicon chip," npj Quantum Inf. **6**, 30 (2020).

[17] A. C. Dada, J. Leach, G. S. Buller, M. J. Padgett, and E. Andersson, "Experimental high-dimensional two-photon entanglement and violations of generalized bell inequalities," Nat. Phys. **7**, 677 (2011).

[18] X.-L. Wang, X.-D. Cai, Z.-E. Su, M.-C. Chen, D. Wu, L. Li, N.-L. Liu, C.-Y. Lu, and J.-W. Pan, "Quantum teleportation of multiple degrees of freedom of a single photon," Nature **518**, 516 (2015).

[19] Z.-F. Liu, C. Chen, J.-M. Xu, Z.-M. Cheng, Z.-C. Ren, B.-W. Dong, Y.-C. Lou, Y.-X. Yang, S.-T. Xue, Z.-H. Liu, W.-Z. Zhu, X.-L. Wang, and H.-T. Wang, "Hong–Ou–Mandel interference between two hyperentangled photons enables observation of symmetric and antisymmetric particle exchange phases," Phys. Rev. Lett. **129**, 263602 (2022).

[20] F. Kaneda, H. Suzuki, R. Shimizu, and K. Edamatsu, "Direct generation of frequency-bin entangled photons via two-period quasi-phase-matched parametric downconversion," Opt. Express **27**, 1416 (2019).

[21] P. Zhao, M.-Y. Yang, S. Zhu, L. Zhou, W. Zhong, M.-M. Du, and Y.-B. Sheng, "Generation of hyperentangled state encoded in three degrees of freedom," Sci. China-Phys. Mech. Astron. **66**, 100311 (2023).

[22] S. Francesconi, A. Raymond, R. Duhamel, P. Filloux, A. Lemaître, P. Milman, M. I. Amanti, F. Baboux, and S. Ducci, "On-chip generation of hybrid polarization-frequency entangled biphoton states," Photonics Res. **11**, 270 (2023).

[23] Z.-D. Liu, O. Siltanen, T. Kuusela, R.-H. Miao, C.-X. Ning, C.-F. Li, G.-C. Guo, and J. Piilo, "Overcoming noise in quantum teleportation with multipartite hybrid entanglement," Sci. Adv. **10**, eadj3435 (2024).

[24] T. Zhong, H. Zhou, R. D. Horansky, C. Lee, V. B. Verma, A. E. Lita, A. Restelli, J. C. Bienfang, R. P. Mirin, T. Gerrits *et al.*, "Photon-efficient quantum key distribution using time–energy entanglement with high-dimensional encoding," New J. Phys. **17**, 022002 (2015).

[25] A. Seri, D. Lago-Rivera, A. Lenhard, G. Corrielli, R. Osellame, M. Mazzera, and H. de Riedmatten, "Quantum storage of frequency-multiplexed heralded single photons," Phys. Rev. Lett. **123**, 080502 (2019).

[26] S.-H. Wei, B. Jing, X.-Y. Zhang, J.-Y. Liao, H. Li, L.-X. You, Z. Wang, Y. Wang, G.-W. Deng, H.-Z. Song *et al.*, "Quantum storage of 1650 modes of single photons at telecom wavelength," npj Quantum Inf. **10**, 19 (2024).

[27] H.-H. Lu, M. Liscidini, A. L. Gaeta, A. M. Weiner, and J. M. Lukens, "Frequency-bin photonic quantum information," Optica **10**, 1655 (2023).

[28] H.-H. Lu, J. M. Lukens, N. A. Peters, B. P. Williams, A. M. Weiner, and P. Lougovski, "Quantum interference and correlation control of frequency-bin qubits," Optica **5**, 1455 (2018).

[29] H.-H. Lu, J. M. Lukens, B. P. Williams, P. Imany, N. A. Peters, A. M. Weiner, and P. Lougovski, "A controlled-not gate for frequency-bin qubits," npj Quantum Inf **5**, 24 (2019).

[30] P. Imany, J. A. Jaramillo-Villegas, M. S. Alshaykh, J. M. Lukens, O. D. Odele, A. J. Moore, D. E. Leaird, M. Qi, and A. M. Weiner, "High-dimensional optical quantum logic in large operational spaces," npj Quantum Inf. **5**, 59 (2019).

[31] L. Olislager, J. Cussey, A. T. Nguyen, P. Emplit, S. Massar, J.-M. Merolla, and K. P. Huy, "Frequency-bin entangled photons," Phys. Rev. A **82**, 013804 (2010).

[32] M. Kues, C. Reimer, J. M. Lukens, W. J. Munro, A. M. Weiner, D. J. Moss, and R. Morandotti, "Quantum optical microcombs," Nat. Photonics **13**, 170 (2019).

[33] R.-B. Jin, Z.-Q. Zeng, D. Xu, C.-Z. Yuan, B.-H. Li, Y. Wang, R. Shimizu, M. Takeoka, M. Fujiwara, M. Sasaki, and P.-X. Lu, "Spectrally resolved Franson interference," Sci. China-Phys. Mech. Astron. **67**, 250312 (2024).

[34] S. Ramelow, L. Ratschbacher, A. Fedrizzi, N. K. Langford, and A. Zeilinger, "Discrete tunable color entanglement," Phys. Rev. Lett. **103**, 253601 (2009).

[35] R. Xue, X. Yao, X. Liu, H. Wang, H. Li, Z. Wang, L. You, Y. Huang, and W. Zhang, "Spatial quantum beating of adjustable biphoton frequency comb with high-dimensional frequency-bin entanglement," IEEE Photonics J. **11**, 7500109 (2019).

[36] N. Fabre, G. Maltese, F. Appas, S. Felicetti, A. Ketterer, A. Keller, T. Coudreau, F. Baboux, M. I. Amanti, S. Ducci, and P. Milman, "Generation of a time-frequency grid state with integrated biphoton frequency combs," Phys. Rev. A **102**, 012607 (2020).

[37] N. B. Lingaraju, H.-H. Lu, S. Seshadri, P. Imany, D. E. Leaird, J. M. Lukens, and A. M. Weiner, "Quantum frequency combs and Hong–Ou–Mandel interferometry: The role of spectral phase coherence," Opt. Express **27**, 38683 (2019).

[38] C. Chen, C. Xu, A. Riazi, E. Y. Zhu, A. C. B. Greenwood, A. V. Gladyshev, P. G. Kazansky, B. T. Kirby, and L. Qian, "Telecom-band hyperentangled photon pairs from a fiber-based source," Phys. Rev. A **105**, 043702 (2022).

[39] J. Li, C. Yuan, S. Shen, Z. Zhang, R. Zhang, H. Li, Y. Wang, G. Deng, L. You, Z. Wang *et al.*, "Discrete frequency-bin entanglement generation via cascaded second-order nonlinear processes in Sagnac interferometer," Opt. Lett. **48**, 2917 (2023).

[40] C. Chen, Y. Chen, and L. Chen, "Spectrally resolved Hong–Ou–Mandel interferometry with discrete color entanglement," Phys. Rev. Appl. **19**, 054092 (2023).

[41] C. L. Morrison, F. Graffitti, P. Barrow, A. Pickston, J. Ho, and A. Fedrizzi, "Frequency-bin entanglement from domain-engineered down-conversion," APL Photonics **7**, 066102 (2022).

[42] Y. Chen, Q. Shen, S. Luo, L. Zhang, Z. Chen, and L. Chen, "Entanglement-assisted absorption spectroscopy by Hong–Ou–Mandel interference," Phys. Rev. Appl. **17**, 014010 (2022).

[43] Y. Chen, M. Fink, F. Steinlechner, J. P. Torres, and R. Ursin, "Hong–Ou–Mandel interferometry on a biphoton beat note," npj Quantum Inf. **5**, 43 (2019).

[44] C. K. Hong, Z. Y. Ou, and L. Mandel, "Measurement of subpicosecond time intervals between two photons by interference," Phys. Rev. Lett. **59**, 2044 (1987).

[45] R.-B. Jin, Z.-Q. Zeng, C. You, and C. Yuan, "Quantum interferometers: Principles and applications," Prog. Quantum Electron. **96**, 100519 (2024).

[46] Y. Chen, L. Hong, and L. Chen, "Quantum interferometric metrology with entangled photons," Front. Phys. **10**, 892519 (2022).

[47] B. Li, Q.-Q. Li, B. Yuan, R. Dong, S. Zhang, and R.-B. Jin, "Quantum metrology timing limits of biphoton frequency comb," arXiv:2410.16841 [quant-ph].

[48] G. Maltese, M. I. Amanti, F. Appas, G. Sinnl, A. Lemaître, P. Milman, F. Baboux, and S. Ducci, "Generation and symmetry control of quantum frequency combs," npj Quantum Inf. **6**, 13 (2020).

[49] C. Lu, X. Wu, W. Wen, and X.-S. Ma, "Discrete and parallel frequency-bin entanglement generation from quantum frequency comb," Adv. Quantum Technol. **8**, 2400229 (2024).

[50] L. Zhang, C. Cui, J. Yan, Y. Guo, J. Wang, and L. Fan, "On-chip parallel processing of quantum frequency comb," npj Quantum Inf. **9**, 57 (2023).

[51] F. Appas, O. Meskine, A. Lemaître, M. Morassi, F. Baboux, M. I. Amanti, and S. Ducci, "Nonlinear quantum photonics with ALGaAs bragg-reflection waveguides," J. Lightwave Technol. **40**, 7658 (2022).

[52] F. Baboux, G. Moody, and S. Ducci, "Nonlinear integrated quantum photonics with AlGaAs," Optica **10**, 917 (2023).

[53] F. Boitier, A. Orieux, C. Autebert, A. Lemaître, E. Galopin, C. Manquest, C. Sirtori, I. Favero, G. Leo, and S. Ducci, "Electrically injected photon-pair source at room temperature," Phys. Rev. Lett. **112**, 183901 (2014).

[54] P. Abolghasem, J.-B. Han, D. Kang, B. J. Bijlani, and A. S. Helmy, "Monolithic photonics using second-order optical nonlinearities in multilayer-core Bragg reflection waveguides," IEEE J. Sel. Top. Quantum **18**, 812 (2011).

[55] A. Vallés, M. Hendrych, J. Svozilík, R. Machulka, P. Abolghasem, D. Kang, B. J. Bijlani, A. S. Helmy, and J. P. Torres, "Generation of polarization-entangled photon pairs in a Bragg reflection waveguide," Opt. Express **21**, 10841 (2013).

[56] Q. Yang and T. Passow, "Non-ideal quarter-wavelength Bragg-reflection waveguides for nonlinear interaction: Eigen equation and tolerance," Opt. Lett. **45**, 4742 (2020).

[57] R. T. Horn, P. Kolenderski, D. Kang, P. Abolghasem, C. Scarcella, A. D. Frera, A. Tosi, L. G. Helt, S. V. Zhukovsky, J. E. Sipe *et al.*, "Inherent polarization entanglement generated from a monolithic semiconductor chip," Sci. Rep. **3**, 2314 (2013).

[58] X. Jing, C. Qian, X. Zheng, H. Nian, C. Wang, J. Tang, X. Gu, Y. Kong, T. Chen, Y. Liu *et al.*, "Coexistence of multiuser entanglement distribution and classical light in optical fiber network with a semiconductor chip," Chip **3**, 100083 (2024).

[59] X. Jing, C. Qian, C.-X. Weng, B.-H. Li, Z. Chen, C.-Q. Wang, J. Tang, X.-W. Gu, Y.-C. Kong, T.-S. Chen *et al.*, "Experimental quantum byzantine agreement on a three-user quantum network with integrated photonics," Sci. Adv. **10**, eadp2877 (2024).

[60] F. Appas, F. Baboux, M. I. Amanti, A. Lemaítre, F. Boitier, E. Diamanti, and S. Ducci, "Flexible entanglement-distribution network with an ALGaAs chip for secure communications," npj Quantum Inf. **7**, 118 (2021).

[61] F. Appas, O. Meskine, A. Lemaître, J. Palomo, F. Baboux, M. I. Amanti, and S. Ducci, "Broadband biphoton generation and polarization splitting in a monolithic ALGaAs chip," ACS Photonics **10**, 1136 (2023).

[62] C. Qian, H. Tian, X. Jing, Y. Liu, Z. Chen, H. Luo, Y. Du, X. Zheng, T. Chen, Y. Kong *et al.*, "Five-user quantum virtual local area network with an ALGaAs entangled photon source," Sci. China-Phys. Mech. Astron. **68**, 230311 (2025).

[63] A. Lyons, G. C. Knee, E. Bolduc, T. Roger, J. Leach, E. M. Gauger, and D. Faccio, "Attosecond-resolution Hong–Ou–Mandel interferometry," Sci.Adv. **4**, eaap9416 (2018).

[64] Z. Huang, C. Chen, L. Hong, Y. Chen, and L. Chen, "Ultrasensitive tilt angle measurement using a photonic frequency inclinometer," Opt. Express **31**, 14149 (2023).

[65] L. Hong, X. Cao, Y. Chen, and L. Chen, "Hong–Ou–Mandel interference of spin–orbit hybrid entangled photons," APL Photonics **8**, 126103 (2023).

[66] L. Xu, Z. Liu, A. Datta, G. C. Knee, J. S. Lundeen, Y.-Q. Lu, and L. Zhang, "Approaching quantum-limited metrology with imperfect detectors by using weak-value amplification," Phys. Rev. Lett. **125**, 080501 (2020).

[67] B. Wang, L. Xu, J.-C. Li, and L. Zhang, "Quantum-limited localization and resolution in three dimensions," Photonics Res. **9**, 1522 (2021).

[68] B. Wang, K. Zheng, Q. Xie, A. Zhang, L. Xu, and L. Zhang, "Achieving the multiparameter quantum Cramér–Rao bound with antiunitary symmetry," Phys. Rev. Lett. **133**, 210801 (2024).

[69] A. Abdullah, N. Ebert, and O. Wasenmüller, "Boosting few-shot detection with large language models and layout-to-image synthesis," in *Computer Vision – ACCV 2024: 17th Asian Conference on Computer Vision, Hanoi, Vietnam, 8–12 December 2024,* (Springer-Verlag, Berlin, Heidelberg, 2024), pp. 202–219.

[70] C. Chen, E. Y. Zhu, A. Riazi, A. V. Gladyshev, C. Corbari, M. Ibsen, P. G. Kazansky, and L. Qian, "Compensation-free broadband entangled photon pair sources," Opt. Express **25**, 22667 (2017).

[71] Y. Chen, S. Ecker, S. Wengerowsky, L. Bulla, S. K. Joshi, F. Steinlechner, and R. Ursin, "Polarization entanglement by time-reversed Hong–Ou–Mandel interference," Phys. Rev. Lett. **121**, 200502 (2018).

[72] X.-Y. Chang, D.-L. Deng, X.-X. Yuan, P.-Y. Hou, Y.-Y. Huang, and L.-M. Duan, "Experimental realization of an entanglement access network and secure multiparty computation," Sci. Rep. **6**, 29453 (2016).

[73] T.-M. Zhao, H. Zhang, J. Yang, Z.-R. Sang, X. Jiang, X.-H. Bao, and J.-W. Pan, "Entangling different-color photons via time-resolved measurement and active feed forward," Phys. Rev. Lett. **112**, 103602 (2014).

[74] Y. Chen, S. Ecker, L. Chen, F. Steinlechner, M. Huber, and R. Ursin, "Temporal distinguishability in Hong–Ou–Mandel interference for harnessing high-dimensional frequency entanglement," npj Quantum Inf. **7**, 167 (2021).

[75] Y. Guo, Z.-X. Yang, Z.-Q. Zeng, C. Ding, R. Shimizu, and R.-B. Jin, "Comparison of multi-mode Hong–Ou–Mandel interference and multi-slit interference," Opt. Express **31**, 32849 (2023).

[76] K. V. Myilswamy and A. M. Weiner, "Spectral compression using time-varying cavities," Opt. Lett. **45**, 5688 (2020).

[77] K. V. Myilswamy, J. A. Gaines, J. D. McKinney, J. M. Lukens, and A. M. Weiner, "From broadband biphotons to frequency combs via spectral compression with time-varying cavities," arXiv:2410.24188.